

Three-dimensional analysis of crack geometry

T. Zhang and G. Nagy

Dept. of Electrical, Computing, and Systems Engineering, Rensselaer Polytechnic Institute, Troy, New York, 12180, USA

E. N. Nagy and E. N. Landis

Dept. of Civil & Environmental Engineering, University of Maine, Orono, Maine, 04469, USA

ABSTRACT: Two types of methods, a threshold-based method and a motion-based method, are applied to recovering and analyzing the cracks in X-ray microtomographic concrete images. The motion-based method provides better results than the threshold-based method. The recovered surfaces of segments and cracks are used for statistical measurement and interactive visualization.

1 INTRODUCTION

Concrete and mortar are quasi-brittle, heterogeneous materials whose fractures are characterized by a wide range of physical processes (van Mier 1997). Although it is known that the microstructural process ultimately governs the fracture behavior, it has typically been ignored because “understanding of this problem is particularly weak at present” (Bazant 1995). Due to the lack of good experimental microstructure data, previous research in fracture modeling aimed to understand and predict only the bulk fracture response.

The application of X-ray microtomography (Flannery et al. 1987; Deckman et al. 1991) can generate multiple volumetric representations of the internal structures of a concrete specimen during its fracture evolution under a metered loading process at an unprecedented resolution (Landis et al. 1999). Although previous studies of fracture energy in 2D and 3D were conducted at a much lower resolution, they did demonstrate that two-dimensional models are not effective in investigating concrete, which exhibits complex 3D fracture surfaces (Nagy et al. 2003).

We study the fractures of concrete by analyzing X-ray microtomographic images using the techniques of image processing. The major advantage is the capability of extracting and analyzing the fractures inside a particular specimen with a certain composition of microstructure.

Two types of methods, a threshold-based method and a motion-based method, have been explored. The motion-based method, which captures distinct

motions of fracture segments, allows depicting their boundaries much more accurately than the alternative method of intensity-based thresholding. By extracting the 3D polygonal models of crack surfaces, a key statistic in fracture analysis, the surface area of cracks, can be computed directly. This statistic is important as it equals the work-of-fracture according to Griffith-type analysis (Broek 1986). These polygonal surface models are also suitable for visualizing 3D crack surfaces interactively. Most previous research on fracture modeling has been largely based on 2D measurement of crack length.

We will first discuss the threshold-based method in Section 3. The motion-based method is explained in Section 4. The results from the motion-based method are presented in Section 5.

2 THRESHOLD-BASED METHOD

In the threshold-based method, cracks are analyzed by thresholding followed by connected component (CC) analysis (Ronse and Devijver 1984; Samet 1989; Borgefors et al. 1997). We applied a robust CC algorithm developed by Franklin (Franklin 1999) that is both space and time-efficient. In testing a concrete data set of size 800 x 800 x 765 (489,600,000 voxels), it finds six million six-connected components in 200 seconds (400 MHz Pentium with 640Mbytes of RAM), with about one third of the time spent on I/O. In addition to listing every connected component with its constituent voxels, the program reports the volume, surface area (number of free faces) and the number of foreground

runs in each component. Based on this connected-component analysis implementation, some routines were developed to analyze the volume distribution, the histogram of free surfaces, and the surface area to volume ratio of the largest components. Most of the statistical results can be found in (Nagy et al. 2001).

This method yields over one million connected components at each threshold. The excessive number of connected components was caused by the non-uniform intensity of the material, the many dark micro-cracks and air-holes, and the side effect of long cracks being divided into shorter cracks at constrictions narrower than the point-spread function of the imaging system. Although we were able to derive some information about the bulk growth of crack volume and tortuosity under load, visualization of so many small connected components with convoluted boundaries was slow and yielded little insight into their structure.

Since this approach processes each image individually, the large number of connected components also makes it difficult to compare or find consistencies between the results from different images. We therefore developed a new method based on motion.

3 MOTION-BASED METHOD

In the motion-based method, the cracks are recovered in three phases: (a) preprocessing, which extracts the concrete region of interest, (b) motion estimation, which estimates a 3D displacement vector field from pairs of images, and (c) motion segmentation, which recovers multiple fractured concrete segments by grouping the displacement vectors according to the principle of Minimum Description Length (MDL) (Rissanen 1978). For measurement of surface area and visualization, the triangulated surface meshes of multiple fragments and cracks are generated with the Marching Cubes algorithm (Lorenson and Cline 1987). For efficiency, the last two steps are iterated in a multi-resolution scheme that takes advantage of results at a lower resolution to process the data at the next higher resolution. Each phase is briefly discussed in the following. Additional details can be found in Zhang (2004).

3.1 Preprocessing

The images in the original concrete sequence are of different sizes. They also exhibit large areas of dark background without concrete. In preprocessing, we first crop each image to a uniform size, large enough to cover all of the concrete region, by resampling around the centroid.

To prevent motion estimation in the void region outside the concrete, a ‘shrink-wrapping’ procedure, implemented using a fast-marching level set method (Malladi et al. 1995), is applied slice by slice. Figure 1 displays several snapshots of shrink-wrapping one sample slice. This model-based segmentation preserves the protrusions and indentations on the boundary of objects. The largest connected components from every slice are stacked together and form the concrete region of interest.

3.2 Estimation of 3D Displacement Vector Field

A block-matching method is applied to estimate 3D displacement vectors using intensity-based registration. Each displacement vector is estimated by finding the maximum normalized cross correlation between a correlation window in the first image, and a same-sized region in a larger search window in the second image.

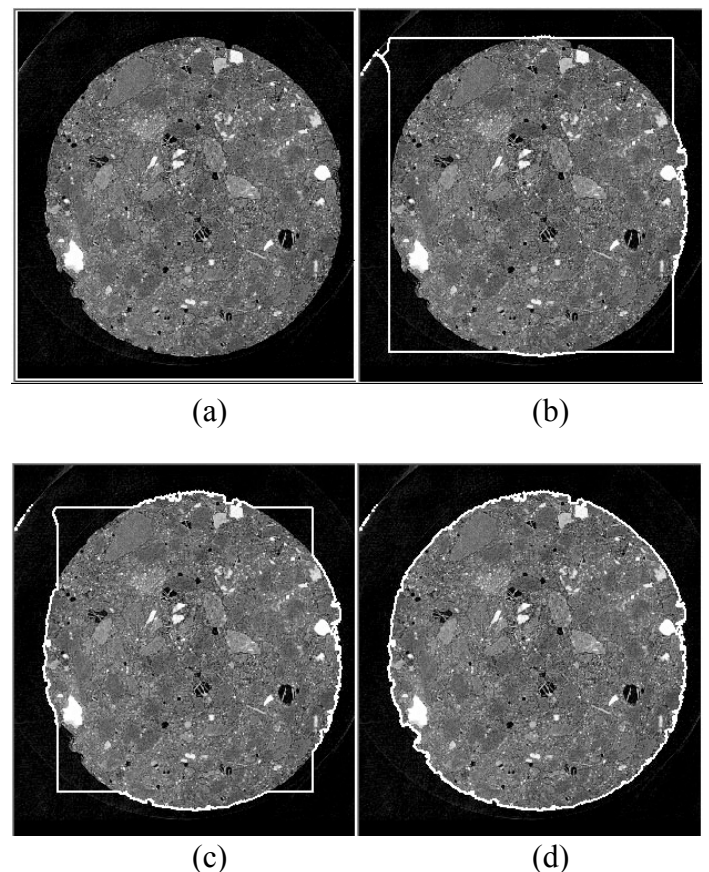


Figure 1. A fast-marching level set method extracts the material region by shrink-wrapping the contour at each iteration until it reaches an edge with high gradient: (a) the contour at initialization; (b) the contour after 2400 iterations; (c) the contour after 4800 iterations; (d) the contour after convergence.

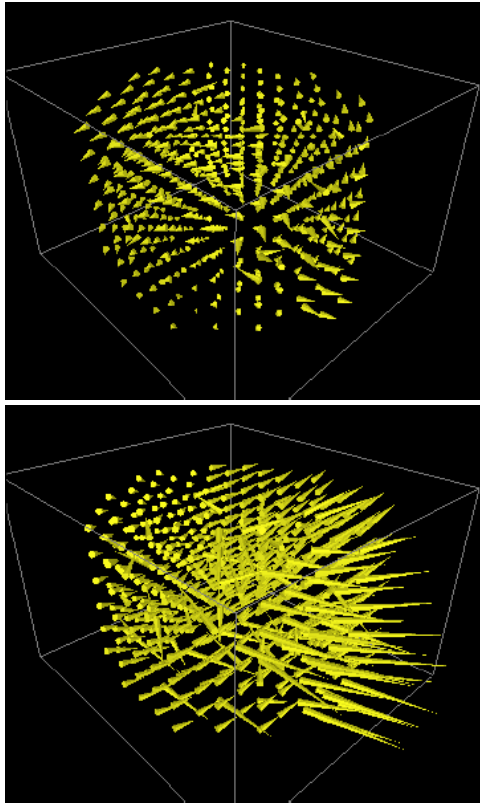


Figure 2. Sample 3D displacement vector fields with small and large motions. The height of directional cones is proportional to the amplitude of the displacement vectors, and is magnified for viewing.

Sequential similarity detection algorithms (SSDAs) were developed by Barnea and Silverman (Barnea and Silverman 1972) to achieve fast computation by calculating the sum of absolute differences between pixel pairs. In adapting SSDAs to 3D, we further improved their efficiency by restricting the number of voxels used in the search window and the size of the search space. Figure 2 shows two examples of sparsely estimated 3D displacement vector fields.

3.3 Grouping of Displacement Vectors

The neighboring locations in the same object undergo the same or similar motions, while those in different objects have distinct motions. We iteratively cluster the displacement vectors according to the principle of Minimum Description Length (Rissanen 1978) to achieve segmentation.

- 1 Start with each voxel as a single connected component whose motion parameter is based on its displacement vector. Calculate the total description length.

- 2 Try merging every pair of neighboring connected components that collide under motion. For every candidate merge, re-estimate the motion model parameters and calculate the change in total description length.
- 3 If the largest change among all candidate merges decreases the total description length, replace the minimum description and reiterate. Otherwise, the procedure ends.

Two constraints are applied during grouping to ensure valid segmentation. Connectivity Constraint: each recovered object must be a connected component. Motion Constraint: Objects cannot collide or inter-penetrate as one object splits into multiple objects with individual motions (Figure 3).

The connectivity constraint is satisfied by the structure of the algorithm because every merge of two neighboring connected components becomes another connected component. To preserve topological integrity, different connectivity must be used for foreground and background. We postulate cubical voxels, face-connectivity for foreground, and vertex-connectivity for background. Edge-connectivity is not used.

The motion constraint is satisfied because the connected components that collide tend to be merged. The implementation of collision detection between connected components is based on Gottschalk's simple and efficient solution that uses the separating axis theorem to detect whether two 3D rectangular bounding boxes collide (Gottschalk et al. 1996).

3.4 Multi-Resolution Scheme

We first sparsely estimate a displacement vector field and recover the fragmented concrete segments

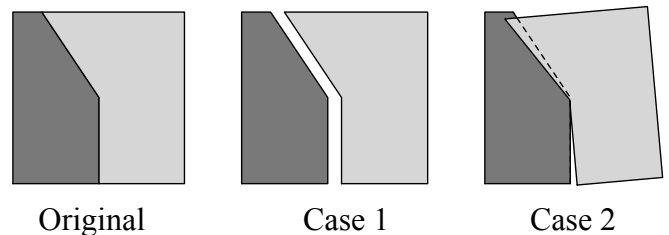


Figure 3. Motion and connectivity constraints as a result of object fragmentation: Case 1 is a possible situation where two child objects move apart; Case 2 is an impossible situation where two child objects inter-penetrate. Each child object is one connected component.

at a low resolution. This coarse result is then used to estimate the displacement vector field at the higher resolution and to update the boundary surfaces of fragmented objects. This process continues until reaching the highest resolution.

The multi-resolution scheme greatly improves processing efficiency on large 3D concrete data sets for several reasons. Firstly, the propagation of the displacements, from the lower resolution to their neighborhoods at higher resolutions, provides accurate initial estimates of the displacement vectors. Secondly, collision between two connected components needs to detect only the neighboring voxels at the lower resolution, and only the collision regions at the higher resolution. Thirdly, interior voxels are assigned to the same object directly, without any MDL calculation.

4 RESULTS

Sequence-B, composed of four images, is used for testing. We refer to each image as B1, B2, B3 and

B4. B1 has no cracks. Widening cracks are observable from B2 to B4. The size of each preprocessed image is 704 x 768 x 512. Because the specimen crumbles near the top and bottom, the fractures are detected only between slices 64 and 448. Each test starts at the lowest resolution, where the fractured objects are identified based on a displacement vector field sparsely estimated at every 64th voxel position. Then the boundary surfaces of fragments are updated based on new displacement vector fields estimated at higher resolutions of every 32nd, 16th and 8th voxel positions. All tests were conducted on a computer with Xeon 2.4G CPU running Linux OS. We intend to push the resolutions even higher, but this will require either multi-day runs or cluster computing.

4.1 Fractured Segments in B2

Two segments are identified, occupying about 64% and 36% of the total volume (Table 1). Their centroids remain stable as the resolution increases. The centroids and relative sizes of these two segments

Table 1. Statistics of the two segments recovered based on the displacement vector field between B1 and B2.

Resolution	64	32	16	8
# Segments	2	2	2	2
Size(%)	63.99 36.01	63.24 36.76	63.35 36.65	65.06 34.94
Centroid (x,y,z)	449,421,246 223,304,275	450,422,252 222,304,264	451,420,253 219,307,260	445,421,255 218,299,258
Surface area of cracks	475558	539469	600997	650349
% of Total surface area	79	76	73	70
Processing time (s)	2	5	91	6315

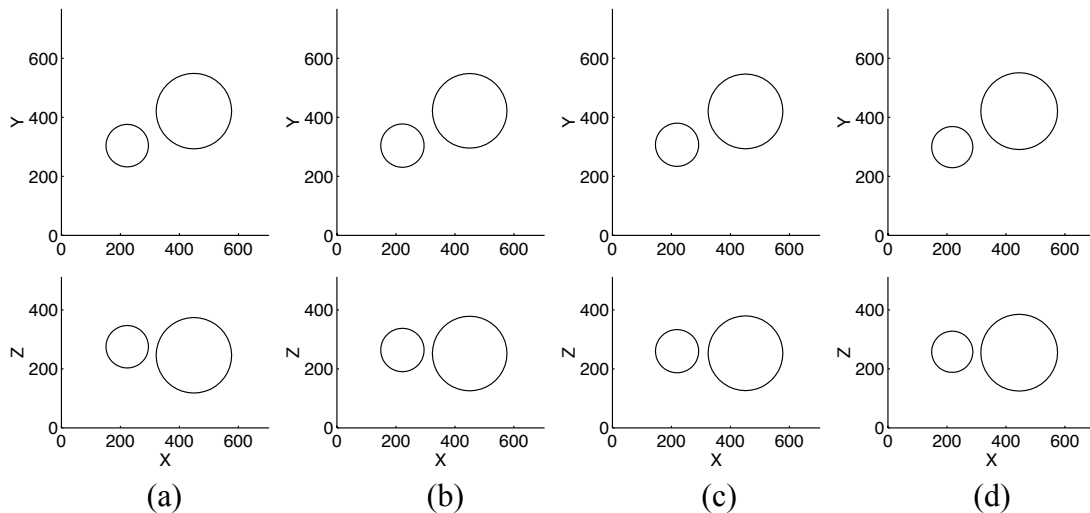


Figure 4. Bubble plots of the two recovered segments in B2 showing their relative sizes and centroids at resolutions of (a) 64; (b) 32; (c) 16; (d) 8.

Table 2. Statistics of the four segments recovered segments in B3.

Resolution	64	32	16	8
# Segments	4	4	4	4
Size(%)	51.74 41.68 4.02 2.56	51.72 42.00 4.32 2.33	51.62 42.01 4.10 2.27	51.44 42.04 4.21 2.31
Centroid (x,y,z)	483,420,254 218,372,262 361,90,291 466,105,155	481,422,255 218,369,261 366,99,269 475,109,155	482,421,256 217,368,260 363,102,269 480,112,166	483,421,255 217,369,260 361,102,263 482,111,177
Surface area of cracks % of Total surface area	570426 100	754281 100	847101 99	921769 99
Processing time (s)	1	5	129	11909

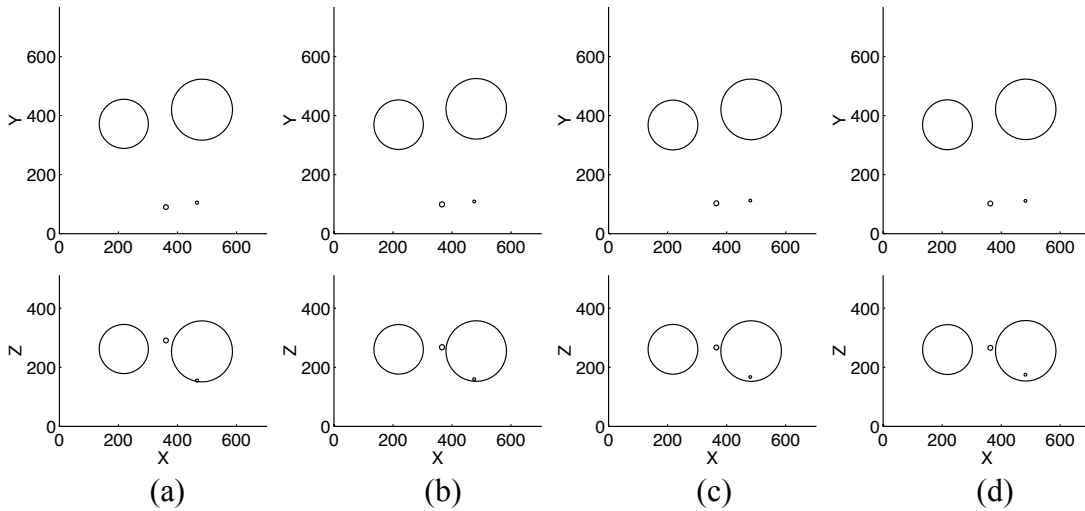


Figure 5. Bubble plots of the two recovered segments in B3 showing their relative sizes and centroids at resolutions of (a) 64; (b) 32; (c) 16; (d) 8.

are better illustrated by a bubble plot (Figure 4), where the area of each circle is proportional to the object size, and the center is at the object centroid. Since objects are in 3D, we have two plots for each resolution, projected on the XY and XZ planes.

The total crack surface area includes two parts: crack surfaces, where the concrete - concrete segments have been separated, and non-crack surfaces, where concrete segments are still in contact. The crack surface and its percentage with respect to the total surface area are listed in the table. The fact that 30% of the total surfaces remains in contact indicates that part of the crack between these two segments remains invisible at the resolution of 83 voxels.

4.2 Fractured Segments in B3

Four segments are located at every resolution (Table 2). Among these four segments, the largest two

cover most of the volume. As the resolution increases, their relative sizes stay quite stable, as observed from the bubble plots (Figure 5.). Compared with B2, the percentage of crack surfaces with respect to the total surface area is close to 100%. This indicates that the specimen is almost fully separated with some minor pivotal connections.

4.3 Fractured Segments in B4

Six segments are located at the lowest resolution of 64. At higher resolutions, two more small segments are identified (Table 3). The bubble plots of recovered segments are in Figure 6. Comparing the sizes of the largest four segments with the largest two in B3, it is seen that the largest segment in B3 has been separated and becomes the first and third largest in B4. The second largest in B3 is also separated and becomes the second and fourth largest in B4.

Table 3. Statistics of the recovered segments in B4.

Resolution	64	32	16	8
# Segments	6	8	8	8
Size(%)	33.09	33.09	32.92	33.06
	29.98	29.04	28.91	29.06
	18.65	17.47	17.34	17.31
	11.52	12.66	12.98	12.90
	4.39	2.95	2.91	3.04
	2.38	2.23	2.17	2.17
		1.41	1.60	1.31
		1.14	1.19	1.15
Centroid (x,y,z)	465,511,246	465,515,252	466,513,254	465,512,253
	219,445,267	219,443,264	217,444,264	217,444,264
	515,253,270	520,249,272	522,249,272	523,249,271
	215,194,245	217,198,254	217,198,252	217,199,252
	360,91,283	360,103,200	364,105,210	363,104,214
	473,108,158	476,110,154	481,112,161	481,112,164
		374,93,405	364,367,103	363,353,109
		357,376,107	366,96,406	364,95,405
Surface area of cracks	1035413	1304762	1482249	1633643
% of Total surface area	100	98	96	97
Processing time (s)	1	8	212	9316

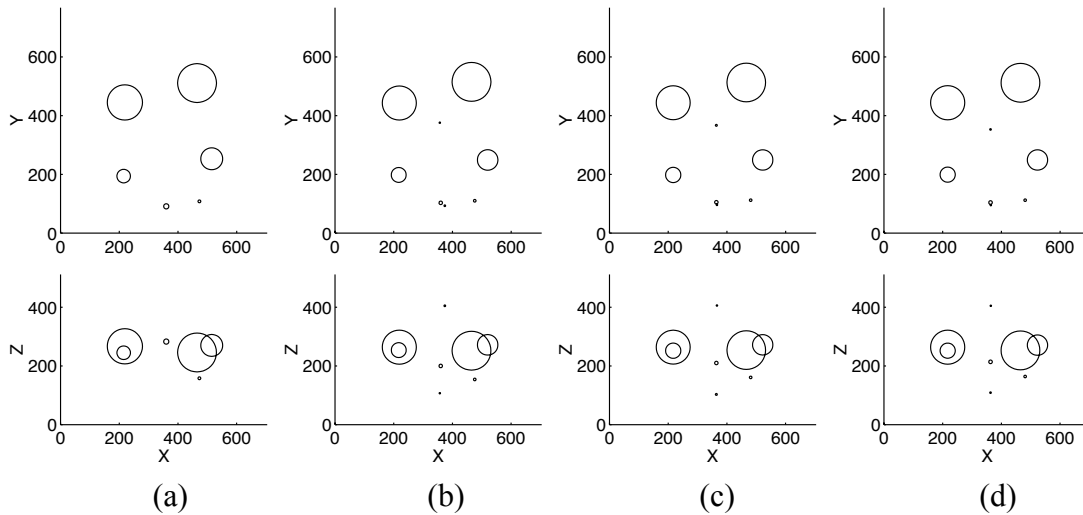


Figure 6. Bubble plots of the two recovered segments in B4 showing their relative sizes and centroids at resolutions of (a) 64; (b) 32; (c) 16; (d) 8.

4.4 Surfaces of Fractured Segments and Cracks

Figure 7 displays the surfaces of fractured segments and cracks at the lowest and highest resolutions. All of these surface models can be visualized interactively. We used a fixed set of colors with good contrast to represent each object. The color is determined by the rank of an object's size.

4.5 Surface Area and Validation

The surface area of cracks in B2, B3, and B4 at different resolutions are summarized and plotted in

Figure 8 (a). Similar trends of increase in the surface area of cracks are observed at every resolution. To validate the accuracy, we first calculate the normalized correlations between each pair of images. Based on the recovered motion parameters, we warp the first image in each pair and re-calculate the normalized correlation between this warped image and the other. The results are plotted in Figure 8 (b). As the specimen breaks apart, the crosscorrelations decrease from 0.83 (B1-B2) to 0.59 (B3-B4) as each separated segments move apart. The increase in cross-correlations to 0.95 (B1-B2) and 0.91 (B3-B4)

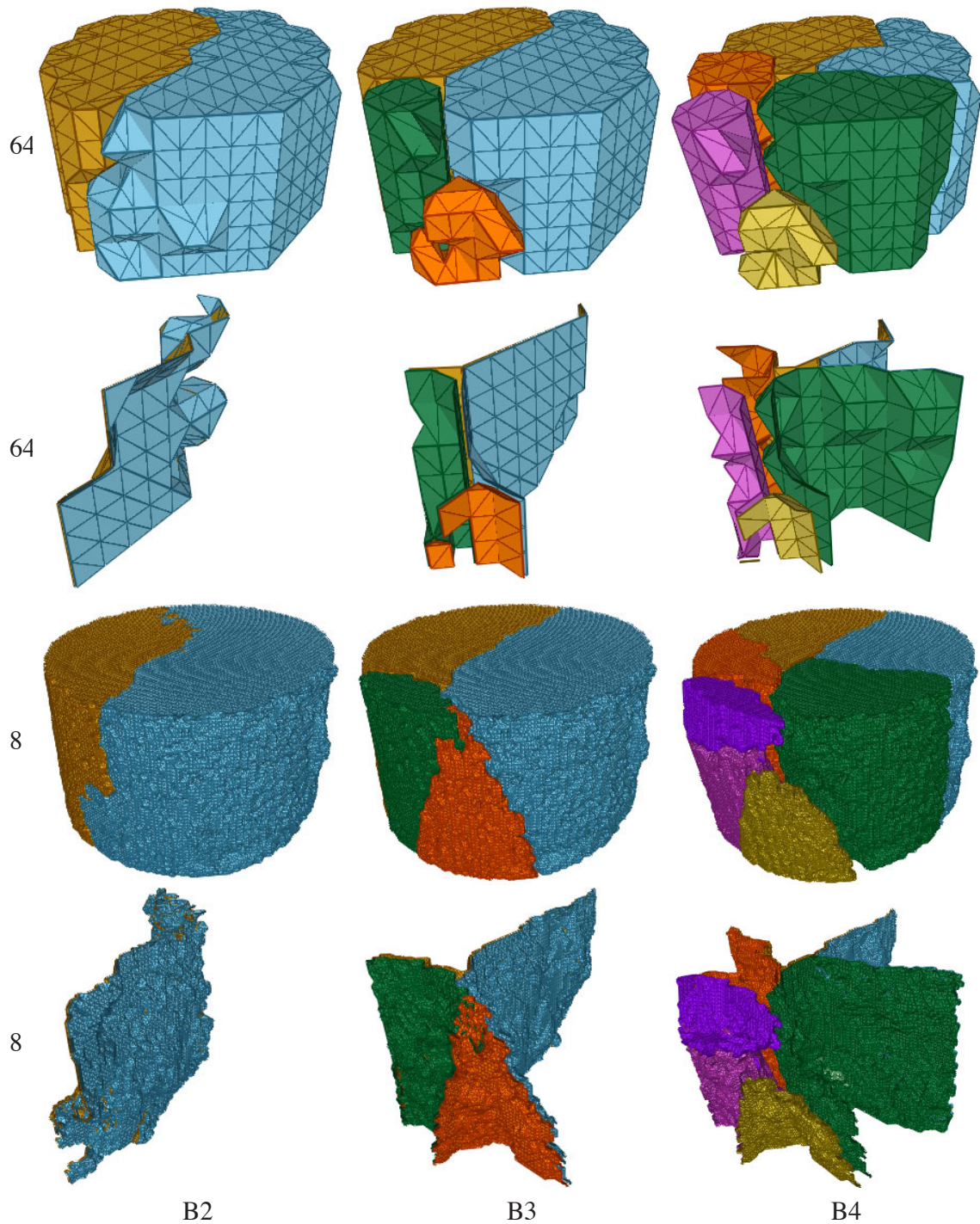


Figure 7. Surfaces of fractured segments and cracks at the lowest and highest resolutions in B2, B3, B4.

at the highest resolution after warping by motion fitting demonstrates the accuracy of the recovered motion parameters.

5 CONCLUSIONS

We have discussed two methods applicable to identification and measurement of the fractured segments

and surface area of cracks. Compared with the threshold-based method, the motion-based method has several advantages: (a) the intensity-based registration in motion estimation does not rely on a specific threshold, and is robust to imaging noise; (b) the motion parameters are estimated accurately based on a large number of globally distributed displacements; (c) the surfaces of latent and narrow cracks, difficult to identify at any threshold, can be

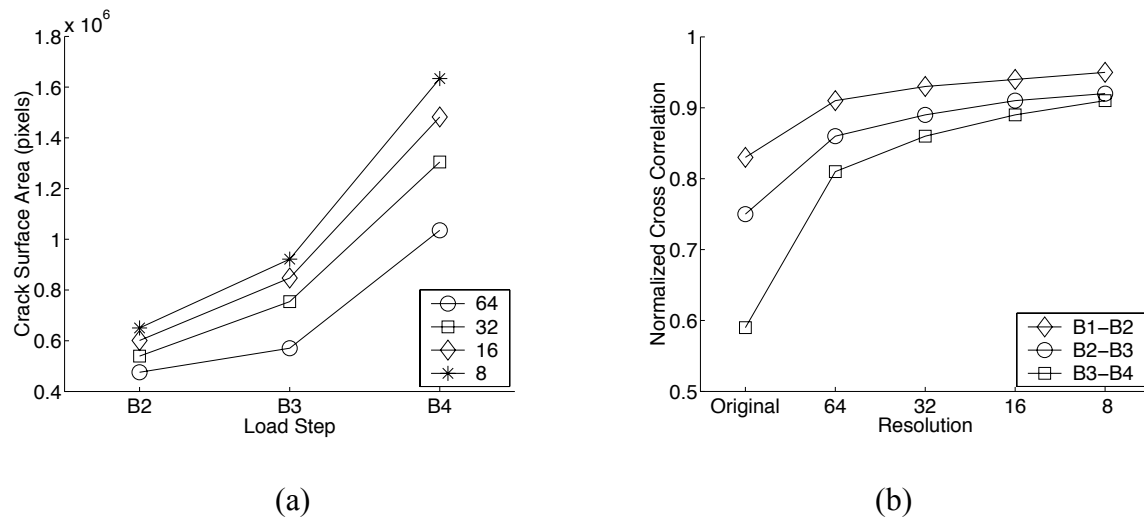


Figure 8. (a) The surface area of cracks at different resolutions in B2, B3, and B4. (b) The normalized cross correlations before and after motion fitting.

inferred by motion interpolation; (d) air holes are not confused with cracks. We have demonstrated that the recovered surfaces of segments and cracks are useful for both statistical measurement and interactive visualization. We will continue working towards better characterization of concrete cracks with respect to the microstructural properties.

6 REFERENCES

- Barnea, D. I. and Silverman, H. F. 1972. A class of algorithms for fast digital image registration. *IEEE Transactions on Computers*, C-21(2): 179–187.
- Bazant, Z. P. (1995). Scaling theories for quasibrittle fracture: recent advances and new directions.” in F. Wittmann ed.), Fracture mechanics of concrete, Proc., 2nd Int. Conf. on Fracture Mech. of Concrete and Concrete Structures (FraMCoS-2), AEDIFICATIO Publishers, 515–534.
- Borgefors, G., Nystrom, I., and de Baja, G. S. 1997. Connected components in 3d neighborhoods. *Procs. 10th Scandinavian Conf. on Image Analysis(SCIA'97), Helsinki*. 557–570.
- Broek, D. 1986. *Elementary engineering fracture mechanics*. Martinus Nijhoff Publishers, Dordrecht, The Netherlands, 4th edition.
- Deckman, H., Dunsmuir, J., D’Amico, K., Ferguson, S., and Flannery, B. 1991. Development of quantitative x-ray microtomography. *Materials Research Society Symposium Proceedings* Vol. 217: 97–110.
- Flannery, B., Deckman, H., Roberge, W., and D’Amico, K. 1987. Three-dimensional x-ray microtomography. *Science*, 237: 1439–1444.
- Franklin, W. R. 1999. Connect - find 3d connected components. <http://www.ecse.rpi.edu/homepages/wrf/research/connect/index.html>
- Gottschalk, S., Lin, M. C., and Manocha, D. 1996. Obbtree: a hierarchical structure for rapid interference detection. *Proceedings of the 23rd Annual Conference on Computer Graphics and Interactive Techniques*. 171–180.
- Landis, E. N., Nagy, E. N., Keane, D. T., and Nagy, G. 1999. Technique to measure 3D work-of-fracture of concrete in compression. *Journal of Engineering Mechanics* 125(6): 599–605.
- Lorensen, W. E. and Cline, H. E. 1987. Marching cubes: a high resolution 3d surface construction algorithm. *ACM Computer Graphics (Proceedings of SIGGRAPH '87)*, 21(4): 163–169.
- Malladi, R., Sethian, J. A., and Vemuri, B. C. 1995. Shape modeling with front propagation: A level set approach. *IEEE Transactions on Pattern Analysis and Machine Intelligence*, 17: 158–175.
- Nagy, E., Zhang, T., Franklin, W. R., and Landis, E. 2003. 3D analysis of tomographic images. *Proc. of 16th ASCE Engineering Mechanics Conference* (electronic), University of Washington, Seattle.
- Nagy, G., Zhang, T., Franklin, W., Landis, E., and Keane, D. 2001. Volume and surface area distributions of cracks in concrete. In C. Arcelli, L. P. Cordella, and G. S. diBaja, (eds.) *Visual Form 2001, 4th International Workshop on Visual Form, Vol. 2059 of Lecture Notes in Computer Science, Capri, Italy*. Springer, 759–768.
- Rissanen, J. 1978. Modeling by shortest data description. *Automatica* (14): 465–471.
- Ronse, C. and Devijver, P. 1984. *Connected components in binary images: the detection problem* Research Studies Press, Letchworth, England.
- Samet, H. 1989. *Applications of Spatial Data Structures* Addison-Wesley.
- van Mier, J. 1997. *Fracture Processes of Concrete* CRC Press, New York.
- Zhang, T. 2004. *Identification of Structural Changes from Volumetric Image Sequence*, PhD Thesis, ECSE Dept, Rensselaer Polytechnic Institute, Troy NY.